Rapid simulation of wide-angle scattering from mitochondria in single cells

Patrick M. Pilarski[a]**, Xuan-Tao Su**[b]**, D. Moira Glerum**[c]**, and Christopher J. Backhouse**[a]*****

[a]*Department of Electrical and Computer Engineering, University of Alberta Edmonton, Alberta, Canada, T6G 2V4.*
[b]*Department of Physics, University of Alberta, Edmonton, T6G 2G7, Canada*
[c]*Department of Medical Genetics, University of Alberta, Edmonton, T6G 2H7, Canada*
Corresponding author: chrisb@ualberta.ca

Abstract: It has been shown that the mitochondria are the dominant source of large-angle light scattering from human cells. In the limit of small mitochondria, we show that the large-angle (isotropic) light scattering of mitochondria may be analyzed and simulated with an adaptation of classical X-ray diffraction theory. In addition, we show that this approach may be extended to the case of anisotropic scatter. These results enable the rapid simulation and analysis of mitochondrial scattering patterns and allow the determination of some aspects of cell structure directly from experimental scattering patterns.

References and links

1. P. L. Gourley, "Biocavity laser for high-speed cell and tumour biology," J. Phys. D-Appl. Phys. **36**, R228–R239 (2003).
2. V. P. Maltsev, "Scanning flow cytometry for individual particle analysis," Rev. Sci. Instrum. **71**, 243–255 (2000).
3. K. A. Sem'yanov, P. A. Tarasov, J. T. Soini, A. K. Petrov, and V. P. Maltsev, "Calibration-free method to determine the size and hemoglobin concentration of individual red blood cells from light scattering," Appl. Opt. **39**, 5884–5889 (2000).
4. Z. Ulanowski, Z. Wang, P. H. Kaye, and I. K. Ludlow, "Application of neural networks to the inverse scattering problem for spheres," Appl. Opt. **37**, 4027–4033 (1998).
5. X.-T. Su, C. Capjack, W. Rozmus, and C. Backhouse, "2D light scattering patterns of mitochondria in single cells," Opt. Express **15**, 10562–10575 (2007).
6. K. Singh, X. Su, C. Liu, C. Capjack, W. Rozmus, and C. J. Backhouse, "A Miniaturized Wide-Angle 2D Cytometer," Cytometry A **69A**, 307–315 (2006).
7. P. L. Gourley and R. K. Naviaux, "Optical Phenotyping of Human Mitochondria in a Biocavity Laser," IEEE J. Quantum Electron. **11**, 818–826 (2005).
8. D. C. Wallace, "Mitochondrial diseases in man and mouse," Science **283**, 1482–1488 (1999).
9. D. C. Wallace, "Diseases of the mitochondrial DNA," Annu. Rev. Biochem. **61**, 1175–1212 (1992).
10. M. Brandon, P. Baldi, and D. C. Wallace, "Mitochondrial mutations in cancer," Oncogene **25**, 4647–4662 (2006).
11. R. Drezek, A. Dunn, and R. Richards-Kortum, "Light scattering from cells: finite-difference time-domain simulations and goniometric measurements," Appl. Opt. **38**, 3651–3661 (1999).
12. R. Drezek, A. Dunn, and R. Richards-Kortum, "A pulsed finite-difference time-domain (FDTD) method for calculating light scattering from biological cells over broad wavelength ranges," Opt. Express **6**, 147–157 (2000).

13. C. Liu, C. E. Capjack, and W. Rozmus, "3-D simulation of light scattering from biological cells and cell differentiation," J. Biomed. Opt. **10**, 014007 (12 pages) (2005).
14. N. Ghosh, P. Buddhiwant, A. Uppal, K. Majumder, H. S. Patel, and P. K. Gupta, "Simultaneous determination of size and refractive index of red blood cells by light scattering measurements," Appl. Phys. Lett. **88**, 084101 (3 pages) (2006).
15. Y. L. Kim, Y. Liu, R. K. Wali, H. K. Roy, M. J. Goldberg, A. K. Kromin, K. Chen, and V. Backman, "Simultaneous measurement of angular and spectral properties of light scattering for characterization of tissue microarchitecture and its alteration in early precancer," IEEE J. Quantum Electron. **9**, 243–256 (2003).
16. H. Fang, M. Ollero, E. Vitkin, L. M. Kimerer, P. B. Cipolloni, M. M. Zaman, S. D. Freedman, I. J. Bigio, I. Itzkan, E. B. Hanlon, and L. T. Perelman, "Noninvasive sizing of subcellular organelles with light scattering spectroscopy," IEEE J. Quantum Electron. **9**, 267–276 (2003).
17. A. Katz, A. Alimova, M. Xu, E. Rudolph, M. K. Shah, H. E. Savage, R. B. Rosen, S. A. McCormick, and R. R. Alfano, "Bacteria size determination by elastic light scattering," IEEE J. Quantum Electron. **9**, 277–287 (2003).
18. J. D. Wilson, C. E. Bigelow, D. J. Calkins, and T. H. Foster, "Light scattering from intact cells reports oxidative-stress-induced mitochondrial swelling," Biophys. J. **88**, 2929–2938 (2005).
19. J. D. Wilson, W. J. Cottrell, and T. H. Foster, "Index-of-refraction-dependent subcellular light scattering observed with organelle-specific dyes," J. Biomed. Opt. **12**, 014010 (10 pages) (2007).
20. C. F. Bohren and D. R. Huffman, *Absorption and scattering of light by small particles* (Wiley, New York, 1998).
21. P. L. Gourley, J. K. Hendricks, A. E. McDonald, R. G. Copeland, K. E. Barrett, C. R. Gourley, and R. K. Naviaux, "Ultrafast nanolaser flow device for detecting cancer in single cells," Biomed. Microdevices **7**, 331–339 (2005).
22. J. S. Modica-Napolitano and K. Singh, "Mitochondria as targets for detection and treatment of cancer," Expert Rev. Mol. Med. **4**, 1–19 (2004).
23. L. J. Garcia-Rodriguez, "Appendix 1. Basic properties of mitochondria," Methods Cell Biology **80**, 809-812 (2007).
24. I. E. Scheffler, *Mitochondria* (John Wiley & Sons, New York, 1999).
25. J. R. Mourant, J. P. Freyer, A. H. Hielscher, A. A. Eick, D. Shen, and T. M. Johnson, "Mechanisms of light scattering from biological cells relevant to noninvasive optical-tissue diagnostics," Appl. Opt. **37**, 3586-3593 (1998).
26. B. Shao, J. S. Jaffe, M. Chachisvilis, and S. C. Esener, "Angular resolved light scattering for discriminating among marine picoplankton: modeling and experimental measurements," Opt. Express **14**, 12473–12484 (2006).
27. K. Singh, C. Liu, C. Capjack, W. Rozmus, and C. J. Backhouse, "Analysis of Cellular Structure by Light Scattering Measurements in a New Cytometer Design Based on a Liquid-Core Waveguide," IEE Proc.-Nanobiotechnol. **151**, 10–16 (2004).
28. T. Proffen and R. B. Neder, "DISCUS: A program for diffuse scattering and defect-structure simulation," J. Appl. Crystallogr. **30**, 171–175 (1997).
29. S. Hoppins, L. Lackner, and J. Nunnari, "The Machines that Divide and Fuse Mitochondria," Annu. Rev. Biochem. **76**, 751-780 (2007).
30. A. K. Dunn, "Light Scattering Properties of Cells," Ph.D dissertation, University of Texas at Austin (1997).
31. P. Pilarski and C. Backhouse, "A method for cytometric image parameterization," Opt. Express **14**, 12720–12743 (2006).
32. E. Hecht, *Optics*, 4th ed. (Addison Wesley, San Francisco, 2002).
33. N. Kasai and M. Kakudo, *X-Ray Diffraction by Macromolecules* (Springer, New York, 2005).
34. P. Thibault, V. Elser, C. Jacobsen, D. Shapiro, and D. Sayre, "Reconstruction of a yeast cell from X-ray diffraction data," Acta Crystallogr. A **62**, 248–261 (2006).
35. J. M. Zuo, I. Vartanyants, M. Gao, R. Zhang, and L. A. Nagahara, "Atomic resolution imaging of a carbon nanotube from diffraction intensities," Science **300**, 1419–1421 (2003).
36. D. Shapiro, P. Thibault, T. Beetz, V. Elser, M. Howells, C. Jacobsen, J. Kirz, E. Lima, H. Miao, A. M. Neiman, and D. Sayre, "Biological imaging by soft X-ray diffraction microscopy," Proc. Natl. Acad. Sci. U.S.A. **102**, 15343–15346 (2005).
37. R. B. Neder and T. Proffen, "Teaching diffraction with the aid of computer simulations," J. Appl. Crystallogr. **29**, 727–735 (1996).
38. T. Proffen and R. B. Neder, "DISCUS: A program for diffuse scattering and defect-structure simulation - update," J. Appl. Crystallogr. **32**, 838–839 (1999).
39. R. Rizzuto, P. Pinton, W. Carrington, F. S. Fay, K. E. Fogarty, L. M. Lifshitz, R. A. Tuft, and T. Pozzan, "Close contacts with the endoplasmic reticulum as determinants of mitochondrial Ca2+ responses," Science **280**, 1763-1766 (1998).

1. Introduction

Previous work has shown that the light scattered by biological cells can be used to infer some aspects of internal cellular structure [1–5]. This is pertinent to emerging wide-angle cytom-

etry systems (currently under development, *e.g.* Singh *et al.* [6]) where the rich structure of two-dimensional scattering signatures from single cells may be used to explore the micro- and nano-structural makeup of the scattering source [5, 6]. Structural information on the intracellular components (such as the organization and number of mitochondria) has great clinical relevance, as it may be used to detect and characterize certain diseases, such as cancer [7–10] and cardiomyopathy [8]. There is a great need for analysis and simulation methods to describe the relationship between experimental scattering patterns and cell structure.

A number of groups have recently worked on the assessment of scatter structure from light intensity measurements or predictions, and these studies typically fall into two categories: *forward methods* and *reverse methods*. Forward methods rely on the prediction of a scattering pattern based on a knowledge of the scattering structure and model of light propagation (*e.g.* Finite Difference Time Domain (FDTD) simulations, [11–13]), while reverse methods attempt to deduce some aspect of scatterer geometry from a pattern of scattered light (again using a model or algorithm to relate pattern to structure). A true reverse method (*i.e.* a direct solution to the inverse scattering problem) would give an exact and detailed geometric structure of a cellular scatterer from a pattern of scattered light. Such a direct reverse solution has been shown to be computationally intractable for the problem of biological cells [2]. However, some advances in the reverse domain have been able to extract one or two physical aspects of the scatterer. Of note, an 'indicatrix' has been used on one-dimensional scattering slices and collections of angular slices to determine cell size and haemoglobin content [2–4]. Scattering has also been used to determine red blood cell size and refractive index via a Fourier transform [14]. Other groups have worked on predicting the properties of bulk solutions of multiple scattering bodies using Mie or Rayleigh-Gans (R-G) theory fitting and Light Scattering Spectroscopy (LSS) [15, 16] or elastic/angularly resolved light scattering [17–19].

Due to the complexity of the forward scattering problem, scattering from individual organelles such as mitochondria is typically described in the literature by Mie and R-G theory [17, 18, 20]. While mitochondria have typically been described (and treated) as ellipsoids or spheroids, with diameters in the 400–800nm range and lengths in the 800–3000nm range [21–23], there is in fact a startlingly wide variety of shapes and sizes documented for these organelles [24]. Nevertheless, it has been demonstrated that mitochondria are the primary large-angle scatterers in eukaryotic cells [25].

Simulation methods such as those based on the Mie and R-G theories give some analytical basis for the intensity patterns observed from (*e.g.* intensity banding [6, 26]), but have significant restrictions in their use (*e.g.* for Mie theory, treating scattering bodies as spheroids). More recently, FDTD code—a discretized solution to Maxwell's equation—has been used to predict scattering from cells [13]. While extremely detailed and true to experimental wide-angle cytometry results [5], FDTD is computationally intensive for any wide-angle 2D cell simulation with realistic parameters [5]; such simulations must be run on large super-computer arrays and may take hours or days to generate a simulated pattern [5].

Though there are many forward and reverse simulation methods, as described above, to date the FDTD method appears to be one of the most effective methods capable of generating realistic wide-angle scattering patterns from a three-dimensional cell model [5, 13]. However, this leads to a computational bottleneck when generating large numbers of simulations, and does not provide a computationally tractable solution to the reverse problem of determining scatterer geometry from an experimental scattering pattern. If we hope to characterize and rapidly classify the effect of nano-structural cell components on scattering, another simulation method must be developed.

We show here that we can produce a good approximation to the scattering pattern of small, isotropically-scattering mitochondria by using an adaptation of conventional X-ray diffraction

theory (XRD) which is particularly suitable for "lab on a chip" (LOC) implementation. We also show how this theory may be extended to deal with the scatter patterns arising from collections of mitochondria whose individual scatter patterns are no longer isotropic, and a more general case: combinations of cellular micro– and nano-structures. The XRD framework provides a wealth of tools that could be applied to this problem. Although XRD is commonly thought of in conjunction with large ('infinite') crystalline structures, it is also applicable in cases of finite and non-crystalline structures—much like the situation of scattering from a single cell. Our approach, based on an adaptation of XRD methods, allows for the rapid simulation of scatter patterns, enabling a number of forward and reverse methods. For forward methods, by quickly simulating large libraries of images that approximate the results of cellular and mitochondrial scattering, computer methods could be used to identify key correlations between scattering patterns and initial scatterer structure. These correlations may be used in an experimental situation to rapidly (*e.g.* real-time) predict the nano-structural makeup of a single cell from the scattering pattern captured by a wide-angle cytometer (*e.g.* [6, 27]). For reverse methods, approaches such as the Reverse Monte Carlo (RMC) method [28] can adapt a model to produce a better fit to an experimentally observed scatter pattern. Either approach depends on the availability of an effective and rapid method of calculating the scatter pattern. The present work gives a theoretical basis for such an approach and demonstrates its effectiveness in application to cancer cells. Given the key role that the mitochondria play in apoptosis [29], a process that lies at the heart of preventing tumourigenesis, the method we describe here could serve as an inexpensive and readily accessible cytometric tool for tracking mitochondrial distributions in cells that have or are suspected as having become cancerous.

2. Methods

2.1. A theoretical approach

As described above, the analysis of nanostructural contributions to scattering in complete cells has so far proved quite difficult. However, it is known that organelles in general, and mitochondria in particular, are the dominant cause of large-angle scattering (*i.e.* light scattered perpendicular to the path of the incident light, commonly called side-scatter or large-angle scattering). As we demonstrate in this work, it is therefore possible to rapidly simulate and analyze the important aspects of large-angle cellular scattering by examining the scattering behaviour of mitochondria.

It has been shown that approximately 90% of side-scattered light from human cells is due to the presence of mitochondria [7, 21]. Small structures, such as the mitochondria, readily scatter at large angles and are in fact the dominant cause of intensity artifacts in this angular region [7, 21, 30]. This is due in part to the complex internal structure of mitochondria and their numerous index-of-refraction changes [1, 7]. As seen from recent experimental and simulation work [5], side-scattered light from the mitochondria in human cells (*e.g.* immune system cells such as the Raji cell-line [5]) typically takes the form of small asymmetrical 'blobs' in a two-dimensional scattering pattern, where blob size and spacing is related to the distribution of small scattering bodies within the cell [5, 31]. Conversely, larger cell structures—such as the nucleus and the cell wall—lead to high intensities of forward and back scatter (*i.e.* angles approaching the path of the incident light) [7, 16, 21, 30] and broad intensity banding in scattering images [5].

This is easily understood by examining the scattering regimes present: cellular components much smaller than the incident wavelength will scatter uniformly in all directions (*i.e.* isotropically) or near-isotropically via the Rayleigh (*size* $\ll \lambda$) and Mie regimes (*size* $\leq \lambda$), while larger bodies will scatter along the light path according to geometric transmission (*size* $\gg \lambda$) [32]. For more information, a detailed description of light scattering by human cells is presented by Gourley *et al.* [7].

Given the dominance of mitochondrial scattering in the large-angle domain, as verified by the recent experiments of Su *et al.* [5], we show that it is possible to model isotropic and anisotropic scattering of mitochondria by adapting classical XRD theory. Although this theory can be extended to larger (anisotropic scattering) mitochondria, in the limit of small mitochondria we find that they can be treated in the same way as isotropically radiating electrons in standard XRD. This greatly reduces the computational burden and provides a means of partially solving the inverse problem.

To simplify the discussion, from this point on we will use and refer to the standard XRD terminology and notation presented by Kasai and Kakudo [33]; relevant terms will be redefined as needed to ensure clarity for the reader.

2.2. A basis in X-ray diffraction theory

It can be shown that large-angle cellular light scattering from small mitochondria fulfills the fundamental constraints and assumptions for XRD-like analysis [33]—specifically: *Thompson scattering*—the incident and scattered wavelengths are the same; *Scatterers radiate isotropically*; and *the Fraunhofer approximation*—energy arrives as a plane wave at the receptive field (*i.e.* the detection plane, likely a charge-coupled device (CCD)); and *the kinematical theory of diffraction*—secondary and tertiary scattering interactions (*i.e.* multi-scatter) should be negligible compared to primary scattering and wave interference [33]. First, like XRD, the incident and scattered wavelengths are the same (*i.e.* elastic scattering). Secondly, in the limit of very small mitochondria (*e.g.* sub-wavelength nanostructures, *i.e.* on the order of a $100nm$ in size), side-scatter will be very close to isotropic, especially when observed via a small solid angle in the side-scatter region [7]. Thirdly, for the geometric arrangement of a wide-angle cytometer [5, 6] the distance to the receptive plane (millimetres) is much greater than the distance between scatterers (micron scale), thus fulfilling the Fraunhofer approximation. Finally, for a standard cytometry system, the impact of multi-scatter, especially for a single-cell situation, is expected to be minimal—first order scattering is barely detectable; second order effects will not be detectable.

Given this, we can begin to examine the mitochondrial scattering problem from an XRD perspective. Neglecting a common prefactor, the amplitude measured at a point **s** (on a detecting plane or receptive field, *e.g.* a CCD), of the collective scattering of a set of isotropic scatterers at locations $\mathbf{r}_n$ is given by the 'explicit' formulation:

$$A(\mathbf{s}) = \sum_{n=1}^{N} [\cos(2\pi \cdot |\mathbf{s} - \mathbf{r}_n|) - i\sin(2\pi \cdot |\mathbf{s} - \mathbf{r}_n|)] \tag{1}$$

Where all distances are measured in units of the wavelength, λ. The intensity on the detecting plane can then be described by the magnitude of the recorded amplitude values (*i.e.* the multiplication of complex conjugates [33]: $I(\mathbf{s}) = |A(\mathbf{s})|^2$). As detailed by Kasai and Kakudo, [33], the intensities, $I(\mathbf{s})$ calculated using Eq. (1) are equivalent to those from another 'explicit' calculation of $A(\mathbf{s})$:

$$A(\mathbf{S}) = \sum_{n=1}^{N} \exp\{-2\pi i(\mathbf{S} \cdot \mathbf{r}_n)\} \tag{2}$$

Where $\mathbf{S} = \mathbf{s} - \mathbf{s_0}$, and $\mathbf{s_0}$ is a unit vector that represents the direction of the illuminating beam, **s** is a unit vector that represents the scatter direction of interest and the product $\mathbf{S} \cdot \mathbf{r}_n$ represents the phase shift (or "path difference" [33]) of the detected light along the observation angle [33].

With $\rho(\mathbf{r}) = \sum_{n=1}^{N} \delta(\mathbf{r} - \mathbf{r_n})$, Kasai and Kakudo showed that this can also be written as a volume integral, over v_r (their Eq. (2.13) [33]):

$$A(\mathbf{S}) = \int_0^\infty \rho(\mathbf{r}) exp\{-2\pi i(\mathbf{S}\cdot\mathbf{r})\}dv_r \qquad (3)$$

We see that, in Eq. (3), $A(\mathbf{S})$ is the 'forward' Fourier transform of the scattering distribution $\rho(\mathbf{r})$, and relates directly to the amplitudes $A(\mathbf{S})$ on the receptive field. If we knew $A(\mathbf{S})$ we could take a inverse Fourier transform (in the reciprocal space) to determine the exact position of the scatterers, *i.e.* (Kasai and Kakudo's Eq. (2.14) [33]):

$$\rho(\mathbf{r}) = \int_0^\infty A(\mathbf{S}) exp\{2\pi i(\mathbf{S}\cdot\mathbf{r})\}dv_s \qquad (4)$$

The central challenge of XRD methods is that we cannot record $A(\mathbf{S})$, but only $I(\mathbf{S})$. As such we lose all phase information and the inverse transform cannot be made readily. Nevertheless, the forward transform is useful to allow patterns to be compared and potential structures investigated [28], the discovery of the helical structure of DNA being a famous example. In addition, although this is not our focus here, XRD methods exist to use $I(\mathbf{S})$ to infer $\rho(\mathbf{r})$. This is commonly used to predict macro-molecule and protein structure from scattering and diffraction patterns with the help of phase reconstruction algorithms [34–36] or methods such as the Reverse Monte Carlo method [28]. With such a wealth of tools it is clear that an XRD-like approach to cytometry would have significant benefits.

As pointed out by Proffen and Neder [28], there is often a significant advantage to using one of the above 'explicit' formulations rather than relying on other methods of performing Fourier transforms—in many circumstances these explicit methods are very much less computationally challenging. This is especially the case when dealing with small numbers of scatterers—a situation that readily arises with microfluidics or "lab on a chip" (LOC) approaches that allow the manipulation and interrogation of a single cell. In a single cell, we are able to deal with hundreds (or fewer) scattering centres (*i.e.* mitochondria) and the explicit methods are readily performed on any type of calculation device (rather than needing a supercomputer as for FDTD methods).

2.3. Scattering examples

As a simple visual example of the relationship of the scattering intensities (e.g. from Eq. (3)) to the distribution of scatterers, Fig. 1 shows how changes to spatial distribution ($\rho(\mathbf{r})$, bottom row) affect the spacing of features in the two-dimensional X-ray scattering pattern, $I(\mathbf{S})$, a) through c), of a small 2×2 grid of atoms (*i.e.* 4 atoms in total) with horizontal spacings of $1\mathring{A}$ and vertical spacings of $1\mathring{A}$ (a), $0.5\mathring{A}$ (b), and $0.33\mathring{A}$ (c). This figure was generated using DISCUS, the widely-used X-ray scattering simulator of Proffen and Neder [28,37,38]. DISCUS is a XRD teaching and simulation tool that applies explicit (discrete) Fourier transforms to simulate the scattering from complex bounded (*i.e.* non-infinite and constrained) crystals and collections of atoms [28, 37, 38]. In this example (Fig. 1), as the y-axis spacing between atoms *decreases* by a factor of two and three, from $1\mathring{A}$ to $0.33\mathring{A}$, panels d) through f), y-axis spacing between features in the reciprocal plot (*e.g.* the scattering or Fourier domain) *increases* by a factor of two and three, from $1\mathring{A}^{-1}$ to $3\mathring{A}^{-1}$, panels a) through c). This calculation is equivalent to that of Eq. (3).

2.4. The `mtPatterns` algorithm

With this theoretical background in mind, we now present a novel method to quickly and inexpensively simulate the large-angle scattering from a series of mitochondria-like scatterers. As discussed above, a LOC approach allows us to measure the scatter pattern of the hundreds of mitochondria from a single immobilized cell. Given the finite number of scatterers, it is most
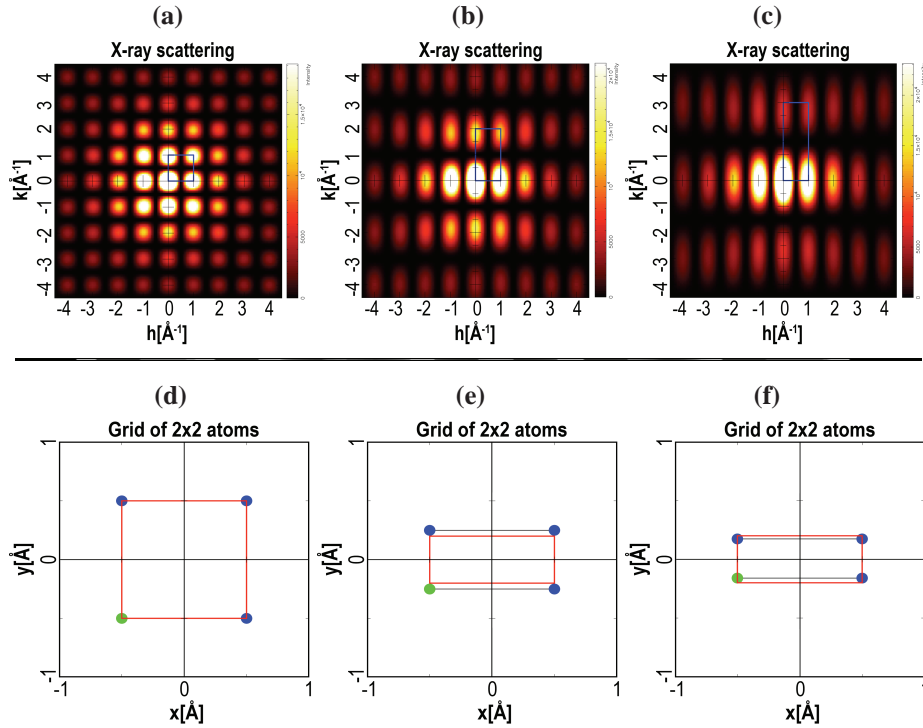
Fig. 1. Example of how changes to the spatial distribution, $\rho(\mathbf{r})$, (d) through (f), impact the spacing of features within two-dimensional scattering patterns, $I(\mathbf{S})$, (a) through (c), in X-ray scattering. As the y-axis spacing between atoms *decreases* by a factor of two and three in panels (e) and (f), y-axis spacing in the reciprocal plot *increases* by a factor of two and three in panels (b) and (c). Physical and Fourier dimensions are listed in $\mathring{A}$ and $\mathring{A}^{-1}$ on the plots above. Data was generated using DISCUS, the Fourier-transform based scattering simulator of Proffen and Neder [28, 37, 38].

appropriate to use an explicit formulation to calculate the scatter, specifically Eq. (1)—*i.e.* we simply sum the radiation from each source within an arbitrary distribution. In essence, it is advantageous to treat the cell as being a disordered crystal of mitochondria.

Overview. The `mtPatterns` algorithm (Tab. 1) is a procedural implementation of Eq. (1), presented and derived in Sec. 2.2. It takes a user-specified distribution of scatterers and generates a two-dimensional scattering plot as its output. Scattering calculation is done by independently summing the isotropic scattering contributions of each scatterer for every point on the receptive field. For the case of anisotropic scattering, a point-spread function may be applied to extend the algorithm to the case of larger spherical or variably-shaped mitochondria.

Algorithm Flow. To begin, the algorithm uses user input to create the scatter distribution and receptive field (steps 1–3). For each point on the receptive field, the algorithm next collects and sums the individual real and imaginary amplitude contributions described in Eq. (1) (steps 4–8). At this point, the amplitude of each scatter may also be scaled by a known point-spread function to compensate for anisotropic scattering (step 7). Finally, the algorithm computes the total intensity value at each pixel, and returns the collected intensity values to the user in image and array form (steps 9–10).

Definitions. The following definitions are used in Tab. 1 and the remainder of this document. $\rho(\mathbf{r})$ is a three-dimensional array of isotropic scatterers (*mt*), created from a user-specified spa-
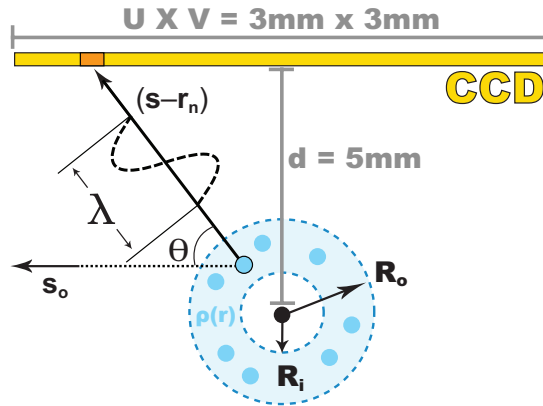
Fig. 2. Diagram of the scattering simulation process. The ray $\mathbf{s_o}$ indicates the direction of incident light, while the segment $(\mathbf{s} - \mathbf{r}_n)$ describes the vector between a scatterer $\mathbf{r}_n$ and a point $\mathbf{s}$ on the receptive filed. R_o and R_i indicate the inner and outer radius of the scattering distribution $\rho(\mathbf{r})$.

tial distribution of scattering points $\mathbf{r}_n$, $n \in [1, \#mt]$. (*n.b.* 'mt' is shorthand for 'mitochondria'.) For this work we assume that the bounds of this distribution are a spherical shell of inside radius R_i and outside radius R_o (*i.e.* the mitochondria are located outside the nucleus of the cell). However, any arbitrary volume may be specified. $\mathbf{I}(u, v)$ is a two-dimensional receptive field created with size $U \times V$ and at a specified distance d along the z-axis away from the scattering population's centroid $\mathbf{r}_o$. A schematic diagram of this setup is shown in Fig. 2. From this point on, we use the vector $\mathbf{s}$ to represent a point on the receptive field with coordinates (u, v, d) from the origin. For scattering computation, A_e and A_m are the real and imaginary amplitude contributions described in Eq. (1), and $M(\theta, \phi, \theta_o, \phi_o)$ is a point-spread function which may be used to scale amplitudes by a known angular distribution. As noted in Sec. 2.2, amplitude calculation is based on $|\mathbf{s} - \mathbf{r}_n|$, the path difference between the observing point $\mathbf{s}$ and the scattering point $\mathbf{r}_n$. $I(\mathbf{s}) = |A(\mathbf{s})|^2 = A_e(\mathbf{s})^2 + A_m(\mathbf{s})^2$ is the summation of real and imaginary amplitude components for each pixel, which form the output intensity profile of the scattering image. To compress the dynamic range of the observed images, we plot the square root $I(\mathbf{s})$.

From this point on we use spherical coordinates to specify location and spacing in the scattering image and related point-spread functions. This allows us to describe patterns in terms of the angle between the path of the incident light and the ray connecting the scattering object to a point on the receptive plane. We define θ as the angle between the scattered light wave vector $(\mathbf{s} - \mathbf{r}_n)$ and the incident light wave vector $\mathbf{s}_o$ (Fig. 2), and ϕ is the angle between the projection of the scattered light wave vector in xy plane and the x axis. For reference, $\theta = 0\,°$ is pure forward scattering, $\theta = 180°$ is pure back scattering. Similarly, $\phi = 0°$ is scattering towards the centre of the receptive field. In the case of spherical scatterers there is no breaking of the symmetry of the system and so there is no ϕ dependence.

For isotropic scatter the above algorithm suffices to calculate $I(\mathbf{s})$. However, as will be discussed below, a number of circumstances can give rise to anisotropic scatter. To allow the calculation of anisotropic scatter we include, as an option, a point-spread function $M(\theta, \phi, \theta_o, \phi_o)$ to allow for scatter in the direction specified by θ and ϕ from a scatterer aligned in a direction specified by θ_o and ϕ_o. The function, $M(\theta, \phi, \theta_o, \phi_o)$, may be applied to scale the isotropic radiation of each scatterer by a known set of angular intensity values (which may be generated numerically [5, 13] or empirically). As will be described below, we have not yet found the need to extend this analysis beyond its application to spherical mitochondria (whether scattering

Table 1. The `mtPatterns` Algorithm

1	Create an array $\rho(\mathbf{r})$ of $0 < n \leq \#mt$ scattering points in $\mathscr{R}^3$ space within bounds $[R_i, R_o]$
2	Create a receptive field $\mathbf{I}$ as an array of size $U \times V$, normal to the z-axis
3	Position receptive field $\mathbf{I}$ distance d above population center $\mathbf{r}_o$ along z axis
4	FOR all $\mathbf{s} \in \mathbf{I}$:
5	FOR $n = [1, \#mt]$:
6	CALCULATE: $A_e(\mathbf{s}, \mathbf{r}_n), A_m(\mathbf{s}, \mathbf{r}_n)$
7	IF non-uniform scattering: $A(\mathbf{s}, \mathbf{r}_n) = A(\mathbf{s}, \mathbf{r}_n) \cdot M(\theta, \phi, \theta_o, \phi_o)$
8	UPDATE: $A_e(\mathbf{s}) + = A_e(\mathbf{s}, \mathbf{r}_n); A_m(\mathbf{s}) + = A_m(\mathbf{s}, \mathbf{r}_n)$
9	$\mathbf{I}(\mathbf{s}) = A_e(\mathbf{s})^2 + A_m(\mathbf{s})^2$
10	Return: $\mathbf{I}$

Takes: $\{\#mt, R_i, R_o, U, V, d, M\}$, Returns: $\{\mathbf{I}\}$

isotropically or anisotropically). As such, we need only consider $M(\theta)$, to allow the simulation of anisotropic scatter from larger, spherical mitochondria. In this work, $M(\theta)$ was a look-up table of real values from 0.0 to 1.0, indexed by the angle θ. Continuous point-spread functions could also be used (*e.g.* from the R-G approximation [17, 18, 20]). Polarisation effects could also serve to break the symmetry to the extent of requiring a $M(\theta, \phi)$ for the simulation of scatter from spherical mitochondria. However, since the present work bases its analysis upon the point-spread functions provided by Gourley *et al.* and these do not contain a ϕ-dependence, we do not presently consider such effects here—although the algorithm could easily do so if the more detailed point-spread functions were available (and needed).

2.5. Effectively isotropic scatter from human mitochondria in the Mie-regime

As discussed by Gourley et al. [21], mammalian mitochondria typically have diameters in the range of 400–800nm. To fall within the realm of true Rayleigh scattering, a structure must be significantly smaller than λ (in this case less than 100nm). Thus, we expect the majority of human mitochondria to scatter in the Mie regime (*i.e.* anisotropically). However, recent work by Gourley *et al.* has shown that mitochondria-like biospheres do in fact exhibit isotropic behaviour up to approximately 500nm in diameter [21].

In their Fig. 1, Gourley *et al.* [21] present their results of using FDTD code to assess the degree of anisotropy that will be produced by spherical mitochondria 100, 500 and 1000nm in diameter. Although we extract quantitative data from those graphs, the uncertainties in doing so are large enough that the results should be interpreted qualitatively. From Gourley *et al.*'s graphs, we see no discernible anisotropy for the 100nm diameter scatterers. For a 500nm mitochondrion, we estimate from that graph that the anisotropic variation seen across a 30-degree-wide cone will be approximately 30%, whereas for the 1000nm diameter mitochondria we estimate a 300% variation over the same range. This small variation for 500nm mitochondria indicates that the scattering behaviour of the mitochondria in human cells is likely to be well modeled by a simulation based on isotropic scatter.

2.6. Test images

Using `mtPatterns`, we created an extensive set of test images and compared them (via qualitative observations and quantitative methods such as comparing characteristic blob spacing) to experimental images generated by a miniaturized cytometry device. These results and comparisons are presented in Sec. 3. In addition to a bank of test images with cell size and nuclear size values $R_o = 0.1\mu m$–$20.0\mu m$ and $R_i = 0.1\mu m$–$20.0\mu m$ (with the number of simulated mi-
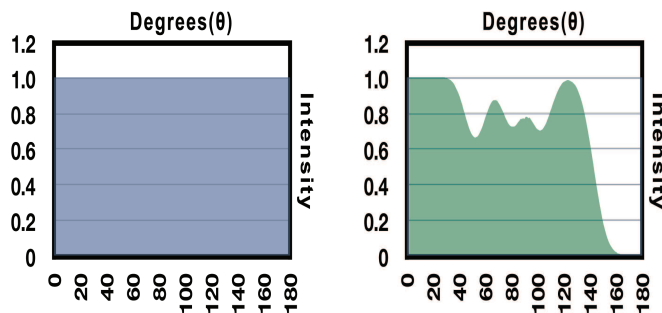
Fig. 3. Two angular point-spread functions $M(\theta)$ for individual scatterers: pure isotropic radiation (left, characteristic of $100nm$ diameter mitochondria (much smaller than λ)), and anisotropic scatter (right, characteristic of 500–$1000nm$ diameter mitochondria)

tochondrial scatters, $\#mt$, varying from 5–1000), additional tests were performed with the specific cell parameters for the Raji human cell line given by Su *et al.* ($R_o \approx 8.0\mu m$, $R_i \approx 4.0\mu m$, $\#mt \approx 83$–677 [5]). This allowed us to explore the behaviour of our algorithm over a wide range of parameters, and also to compare simulations to actual experimental cytometry results for human Raji cells. Each test was performed at least three times with different random placement of mitochondria (with similar results obtained for each).

The following parameters were used in all `mtPatterns` simulations: an incident light wavelength of $\lambda = 632nm$, a CCD receptive field area of $U \times V = 3mm \times 3mm$, with the scatter centroid centered $d = 5mm$ below the CCD plane. These dimensions are much as for the experimental apparatus used by Su *et al.* [5], and can be seen to fulfill the XRD constraints presented in the previous section. Shown in Fig. 2, this setup gives a viewable side-scatter region between $77.3°$ and $106.7°$ in both the θ and ϕ axes (a solid angle corresponding to a cone of $\simeq 30°$).

Two point-spread functions $M(\theta)$ were used: pure isotropic radiation (characteristic of mitochondria and other biospheres smaller than λ [21]) and a theoretical anisotropic point-spread function for a single spherical scatterer (characteristic of larger mitochondria in the Mie scattering regime, as described by the inset of Fig. 1 from Gourley *et al.* [21], or from the polar plots of Fig. 2 of Gourley *et al.* [7]). Although the latter were easier to interpret, these are difficult to extract data from and the behaviours should be taken as qualitatively correct rather than exact. The anisotropic case is from scattering for spherical scatterers in the Mie regime (size $\geq \lambda$, or ~ 500–$1000nm$ in diameter), while the isotropic case is for scatterers in the Rayleigh or near-Rayleigh regime (size $< \lambda$, and up to $\sim 500nm$ [21]). For the anisotropic cases, $M(\theta)$ was used. These point-spread functions are shown in Fig. 3.

3. Results and discussion

The following sections present both a qualitative and a quantitative analysis of the results of applying the `mtPatterns` algorithm, and show that a scattering simulation based only on the distribution of small mitochondria can effectively simulate wide-angle experimental images (recalling that mitochondria are the dominant sources of wide-angle scattering [21]). In XRD, analysis is often done by calculating the Fourier transform of potential crystal structures and comparing them to experimental scattering patterns. We show that a similar process is possible for scattering from mitochondria in a single cell; the following results show the possibility for predictive assessment of cell structure, in this case mitochondrial number and distribution, based on comparison with experimental scatter patterns.

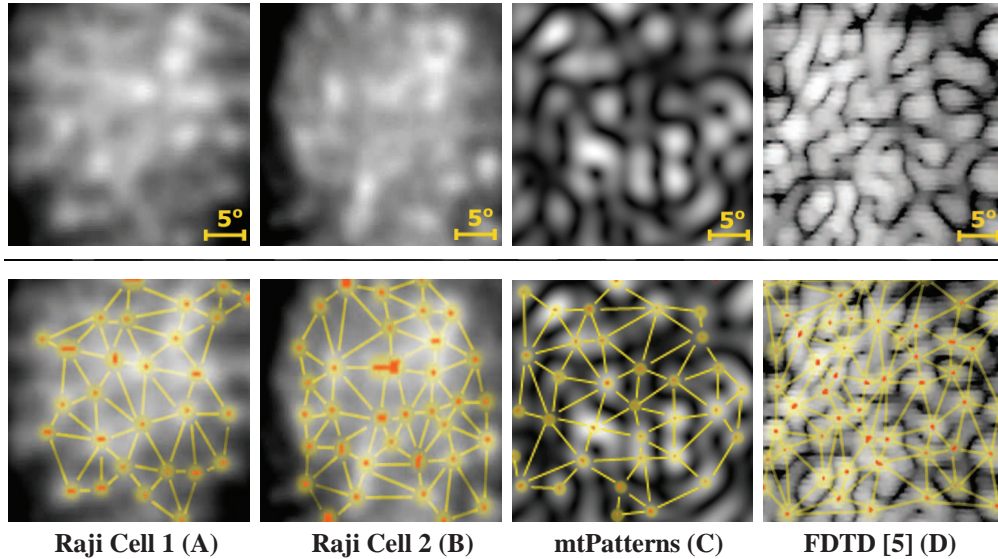**Raji Cell 1 (A)   Raji Cell 2 (B)   mtPatterns (C)   FDTD [5] (D)**

Fig. 4. A comparison of feature spacing between the experimental cytometry data for two Raji cells (A and B, $R_o \cong 8.0\mu m$, $R_i \cong 4.0\mu m$, each with an estimated hundreds of mt), the `mtPatterns` algorithm (C, $R_o = 8.0\mu m$, $R_i = 4.0\mu m$, #mt = 300), and a re-processed version of the FDTD results of Su *et al.*'s Fig. 5(d) [5] (D, $R_o = 8.0\mu m$, $R_i = 4.0\mu m$, #mt = 300) over a 30º range in ϕ and θ, located in the side-scatter region. The point / line overlays in the bottom row indicate blob center points / spacing gaps used in blob spacing calculations. The horizontal axis corresponds to changes in θ, vertical to changes in ϕ.

3.1. *Comparison of* `mtPatterns` *and experimental cytometry images*

To evaluate the `mtPatterns` algorithm, `mtPatterns` results were compared to experimental wide-angle cytometry patterns captured using the method described by Su *et al.* [5] from the laser scattering of human Raji cells. Experimental Raji data was generated by one of the first published demonstrations of a microchip-based wide-angle cytometer [5]. All experimental data was scaled and cropped to the same side-scatter angular range as the `mtPatterns` data (from 77.3° to 106.7° in θ and ϕ, Sec. 2.6, selected to best show the side-scatter effects of the scatter distribution) and normalized to the same intensity and contrast levels. We also performed comparisons with a reprocessed version of the FDTD data published by Su *et al.*, describing a 2*mm* by 2*mm* CCD region with an angular range between $\sim 60°$ to 90° in θ and $\sim 77°$ to 107° in ϕ (their Fig. 5(d), [5], generated from a mitochondrial distribution with many of the same parameters as the `mtPatterns` test, but with a different random seed for organelle placement). FDTD data was cropped and normalized as described above. Estimated cell parameters from the experimental and FDTD data (as per Su *et al.* [5]) were used as input to `mtPatterns` to generate the simulations. This process allowed for direct visual and numerical comparison.

The similarity between images may be visually judged by examining the shape and image structure of scattering images obtained from `mtPatterns` and from real experimental cytometers. Figure 4, top, shows the experimental scattering signatures for two human Raji cells, taken using a miniaturized cytometer, with estimated cellular parameters of $R_o \approx 8.0\mu m$, $R_i \approx 4.0\mu m$, and about 100 to 700 mt, as per the experiments of Su *et al.* [5]. Qualitatively, these patterns are structurally similar—in terms of blob spacing and size (angular size, Fig. 4, top)—to the pattern generated by `mtPatterns` (Fig. 4(c), top) when initialized with the average parameters of a Raji cell estimated by Su *et al.* ($R_o = 8.0\mu m$, $R_i = 4.0\mu m$, #mt = 300).

The `mtPatterns` blob size and spacing also agreed with the re-processed version of Su *et al.*'s [5] FDTD pattern for a random distribution of 300*mt* ($R_o = 8.0\mu m$, $R_i = 4.0\mu m$, no nuclear or cellular scattering, Fig. 4(d), top), though FDTD showed on average a slightly lower characteristic spacing and blob size than both experimental samples and `mtPatterns`.

It is difficult to objectively compare scattering images in quantitative terms [31]. However, since the spacing of the scattering distribution relates to scattering pattern blob spacing (Eqs. (2), (3)), one effective way to numerically compare scattering images is to evaluate their characteristic angular spacing, defined as the average angular distance (in degrees) between neighboring scattering intensity maxima. This metric also can help guide the process of inferring experimental scattering structure from simulated images.

For the numerical comparisons presented here, angular spacing (in image space) between neighbouring maximum intensity regions (*i.e.* blob peaks) was measured as shown by the mesh in Fig. 4 and normalized to the angular range of each image to give a set of angular blob spacing values for each image. These spacing values were then averaged to compute each image's characteristic spacing value and its variability.

Using this metric, we compared the experimental images of Fig. 4 to the `mtPatterns` simulation generated using the corresponding parameters. This comparison can be seen qualitatively in the bottom panels of Fig. 4, and quantitatively as follows. As described above, `mtPatterns` was initialized with the estimated parameters of a Raji cell ($R_o = 8.0\mu m$, $R_i = 4.0\mu m$, #*mt* = 300, as given by Su *et al.* [5]). With these parameters, we observed an average angular spacing (and standard deviation) between the maxima of intensity regions (*i.e.* blob centers) of $5.51 \pm 1.51°$ (73 samples; Fig. 4(c)). This compared well to the spacing values from the experimental cytometry images: $5.12 \pm 1.47°$ (85 samples; *Raji Cell 1*—Fig. 4(a)) and $6.04 \pm 1.46°$ (62 samples; *Raji Cell 2*—Fig. 4(b)). It also was in agreement with the re-processed FDTD results of Su *et al.*: $4.98 \pm 1.63°$ (139 samples; Fig. 4(d)).

As such, the `mtPatterns` characteristic spacing value was observed to be within the range of values from the two experimental cells and the FDTD simulation: spacing FDTD < *Raji Cell 1* < `mtPatterns` < *Raji Cell 2*. The slight variations in average characteristic spacing between the two experimental samples are likely due to changes in internal cell structure (such as mitochondrial number and placement) and are well within one standard deviation. The smaller spacing in FDTD may also be due to modeling differences and the $\theta - 17°$ shift in the observed angular range [5].

Lastly, we found that the experimental results (Fig. 4(a,b)) appeared to have more intensity toward the centre of the image. This background intensity could indicate the contributions of larger cell components and microstructures (*e.g.* the nucleus), light from the experimental setup, and/or the washed-out superposition of any non-uniform mitochondrial scattering (discussed below). As this background consists primarily of broad low-frequency features, they could potentially be separated from, and analysed separately from, the blob-like features. Feature extraction methods (*e.g.* Cythe [31]) may be used to facilitate this.

The combination of the ability to calculate blob spacing and the ability to rapidly generate realistic simulated scattering plots with the `mtPatterns` algorithm facilitates the prediction of mitochondrial spacing directly from an observed scattering image. Once it is possible to quickly simulate realistic mitochondrial scattering patterns, simple visual and numerical comparisons could be used to perform real-time classification of cytometrically interrogated cells. As shown by XRD, great leaps in structural assessment can be made by comparing experimental and simulated scattering patterns.

	1	2	3	4	5

$R_o = 2\mu m$ $R_o = 2\mu m$ $R_o = 8\mu m$ $R_o = 8\mu m$ $R_o = 20\mu m$
$R_i = 1\mu m$ $R_i = 1\mu m$ $R_i = 1\mu m$ $R_i = 1\mu m$ $R_i = 5\mu m$
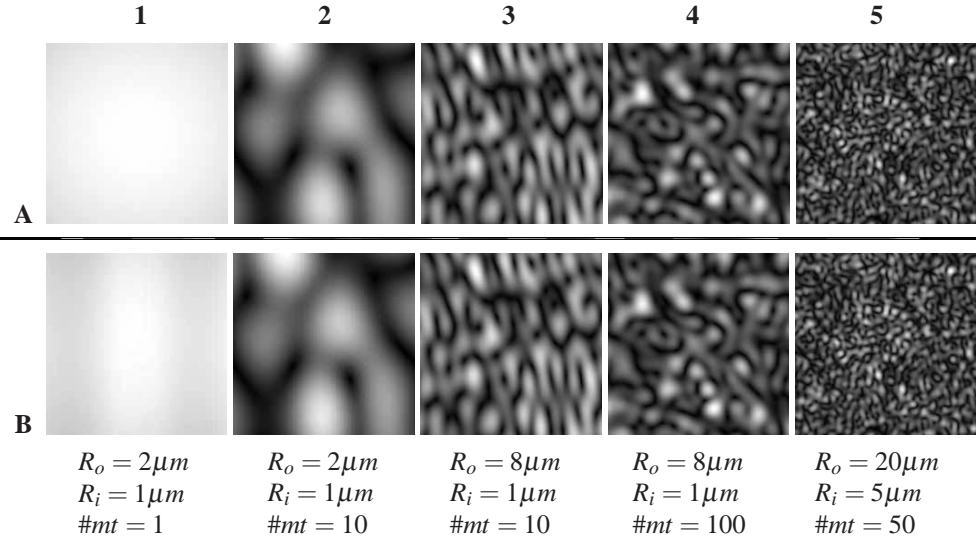$\#mt = 1$ $\#mt = 10$ $\#mt = 10$ $\#mt = 100$ $\#mt = 50$

Fig. 5. A series of sample images generated using the `mtPatterns` algorithm. Images are shown for both uniform scattering (row A) and scattering using a complex point-spread function (row B, as per Fig. 3, right). Increased scatterer spacing can be seen to lead to a decrease in scattering pattern blob spacing (*e.g.* 2A, 3A). In terms of scattering blob placement and spacing, there is little difference between uniform (A) and non-uniform (B) mitochondrial scattering. To allow visual comparison, all images have been normalized with respect to the same minimum and maximum intensity values (*i.e.* 0–255), and cover the same solid angle (77.3°–106.7° in θ and ϕ). Forward scatter is toward the right.

3.2. Extension to non-uniform scattering from larger spherical mitochondria

As discussed and shown above, at least for smaller mitochondria it appears that the scatter can be well-approximated by a model of isotropic scatter. However, the degree of scatter anisotropy becomes far more pronounced for larger mitochondria. We will now show a theoretical basis for extending our simulation approach to deal with arbitrarily large degrees of anisotropy from spherical mitochondria (*i.e.* much larger that $500nm$, when their dimensions exceed the wavelength of the incident light).

Up to now we have dealt with scatter patterns $M(\theta)$ due to ϕ-invariant scatter from spherical mitochondria. More generally, the scatter of a mitochondrion in a direction specified by the vector $\mathbf{S}$ can be written as $M(\mathbf{S})$. Such a scattering pattern from an isolated (larger) mitochondrion, $M(\mathbf{S})$, may be calculated using numerical methods such as FDTD (as done by [21]), R-G, or captured in an experimental situation. This pattern could be the result of energy scattering from a complex substructure in the spatial domain, which we will denote $m(\mathbf{r})$.

From XRD, we know that the scattering pattern of an array of an identical and aligned substructures can be related to the scatter pattern of the sub-structure alone, $m(\mathbf{r})$, and that of the array alone, $\rho(\mathbf{r})$, through the convolution theorem. In the present case $m(\mathbf{r})$ is the sub-structure within a single mitochondrion, while in XRD it is the arrangement of electrons in a single scattering body. This convolution takes the form: $\rho(\mathbf{r}) * m(\mathbf{r})$. The scattering pattern $A_{true}(\mathbf{S})$ of the distribution of mitochondria with complex sub-structure will therefore be the Fourier transform of this convolution, Eq. (5), or, equivalently, the product of the Fourier transform of the array multiplied by the Fourier transform of the sub-structure, Eq. (6). (Although there are likely to be methods in XRD analysis for application to disordered crystals with misaligned substructures, the XRD theory presented in this section is not able to account for misalignments

(*i.e.* ϕ_o and θ_o) in the sub-structure—this type of analysis will be discussed below.)

$$A_{true}(\mathbf{S}) = F\{\rho(\mathbf{r}) * m(\mathbf{r})\} \tag{5}$$

Thus, if $A(\mathbf{S})$ is the transform of the distribution of mitochondria, $\rho(\mathbf{r})$ (assumed to be isotropic scatterers), and $M(\mathbf{S})$ is the transform of isotropic-scattering sub-structure, $m(\mathbf{r})$, within the mitochondria that gives rise to the observed anisotropic behaviour, then the true scatter pattern, $A_{true}(\mathbf{S})$ is:

$$A_{true}(\mathbf{S}) = A(\mathbf{S})M(\mathbf{S}) \tag{6}$$

In the context of XRD, this is discussed in more detail in standard references (such as [33,37]). This approach may be applied to mitochondrial light scattering by noting that an array of mitochondrial positions $\rho(\mathbf{r})$ may therefore be convolved with some internal sub-structure $m(\mathbf{r})$ to account for the anisotropic scatter from the internal sub-structure. However, it is not important to know or guess at $m(\mathbf{r})$, we need only obtain $M(\mathbf{S})$, the scatter pattern of the individual mitochondrion, from FDTD, R-G, or experiment. Since we know the final scattering pattern will be the multiplication of two Fourier transforms, Eq. (6), we can simply use Eq. (2) or (3) to compute the scattering pattern $A(\mathbf{S})$ for a given distribution of isotropically scattering mitochondria $\rho(\mathbf{r})$ and multiply the result by $M(\mathbf{S})$, to obtain the real mitochondrial scattering pattern, $A_{true}(\mathbf{S})$. This shows that the analysis of anisotropic scatter from larger spherical mitochondria, can be done in a way that remains consistent with XRD theory (and hence toolsets).

As shown in Fig. 5, there was little difference between `mtPatterns` scattering images created using isotropic scatterers (Fig. 5(a)) and scatterers with the more complex point-spread functions characteristic of larger mitochondria (Fig. 5(b)). Our experiments showed little structural variation (in terms of scattering blob size, spacing, and intensity) between large-angle scattering patterns generated using a uniform point-spread function (Fig. 3, left) and those generated by radiators using the point-spread function described by Gourley *et al.* (Fig. 3, right). This was expected, as the theoretical point-spread function of a non-isotropic mitochondrion is almost identical to an isotropic point-spread function when observed over a solid angle equivalent to a cone approximately 30° across, centered on the side-scatter region. As such, the use of isotropic scattering points to simulate mitochondria proved experimentally to be a valid first-order approximation in the large-angle scattering domain. In other words, it appears that small variations in scattering intensity with angle do not affect the overall pattern—they are readily 'washed out'. However, if the degree of anisotropy from a spherical scatterer were large enough that we needed to account for it, the above approach would suffice (through the use of our algorithm or by means of an XRD-like method).

3.3.   *Extension to non-uniform scattering from non-spherical mitochondria*

In the above, anisotropic scatter was considered to originate from larger spherical mitochondria. Another source of anisotropy is from non-spherical mitochondria. Although much of the work in the literature has considered the mitochondrion to be an ellipsoid or a sphere, the structure of the mitochondrion is not yet firmly established. Assuming that the mitochondria are not physically correlated in part of a larger structure, we would expect orientations that are random. As such, we would expect less of an overall effect than seen in the case of the larger spherical mitochondria where the anisotropy was a function of θ (and hence correlated). Gourley *et al.* [21] have made a similar suggestion. On the other hand, recent reports suggest that the mitochondria do form an interconnected network, depending on the needs, type and state of the cell [29,39]. A further exploration of this is underway, and will require extensive simulation and an examination of real cells in a variety of states. Much as above, if the degree of anisotropy

from a non-spherical scatterer were large enough (or correlated enough) that we needed to account for it, our algorithm would be able to do so. Since doing so would introduce a large number of new variables (ϕ_o and θ_o for each mitochondrion), it would seem unwise to attempt to do this until the need has clearly been demonstrated.

3.4. *Observations on the effect of scatter distribution and interaction*

Figure 5 also shows that an increase in the number of scatterers lead to increased image complexity (*i.e.* smaller blobs and smaller characteristic spacing). In addition, an increased scatterer distribution radius R_o also led to increased image complexity. A tightly arranged mitochondrial distribution (*e.g.* smaller mitochondrial volume, such as Fig. 5(a2)) resulted in larger homogeneous intensity regions with greater characteristic spacing, while wider distributions (such as Fig. 5(a5)) generated a number of small, tightly spaced intensity regions.

This behaviour is expected from Fourier theory and X-ray diffraction literature, as described above. As in Fourier theory, the spacing between, and size of, intensity regions on the simulated CCD region were inversely proportional to the spacing of the original organelle distribution. The more dense the scattering distribution, the more distance between blobs in the scattering plot (Fig. 5). These trends will be useful in future feature-based classification systems, as image feature complexity can help deduce initial cell structure [31], whether by direct comparison of features or phase reconstruction techniques.

Lastly, when the distribution of scattering points was tightly packed within a volume much smaller than λ, we found that the resulting scattering pattern closely matched that of a single scatterer. Under these conditions, scattering contributions from individual scatterers washed out to form a single bright intensity region. We found this to be true for any number of scatterers. However, the un-normalized intensity of the region increased in proportion to the number of scatters (*#mt*). This result is expected from scattering theory, and has been experimentally corroborated by Gourley et al. [21]; as $R_o \ll \lambda$, scattered phases will align and all scattering contributions will be uniformly constructive regardless of scatterer number. This is also analogous to the scattering for a random array of apertures, shown in Fig. 10.33 of [32]. As such, the un-normalized average intensity of a signature might prove to be a useful predictor of the raw number of mitochondria within a experimental sample; this would allow the classification of both the mitochondrial spacing (through blob spacing, described above) and number (through un-normalized blob intensity) of scattering mitochondria, all from a single scattering plot.

4. Conclusions

In the limit of small mitochondria, we show that large-angle light scattering of mitochondria may be treated using an adaptation of classical X-ray diffraction theory, giving rise to a computationally efficient solution to the scattering simulation problem. In addition, we show that this approach may be expanded to the general case of larger mitochondria which may or may not scatter in an isotropic fashion. This result facilitates the rapid simulation of realistic mitochondrial scattering patterns—without the need for computationally challenging or restrictive routines—and allows the determination of some aspects of cell structure directly from experimental scattering patterns. Large-angle mitochondrial scattering signatures can be calculated in seconds, allowing the rapid creation of large predictive image databases and facilitating great advances in real-time patient care, cell structure prediction, and cell morphology research. In the present work, the computation time of the average `mtPatterns` simulation was between a fraction of a second and a minute on a standard personal laptop computer running the Python interpreter.

Through rapid simulation, the `mtPatterns` algorithm allows the prediction mitochondrial spacing (via scattering pattern blob spacing) and number (via scattering pattern inten-

sity), directly from an observed scattering image. In addition, given the dramatically different scattering contributions of cellular micro– and nano-structures, we show that it is possible to isolate (using, for example, feature extraction methods [31]) just the high-frequency scattering contributions of nanostructres by removing—or separately analyzing for useful diagnostic information—the broad band-like scattering of larger microstructures.

This analogy to XRD and ability to inexpensively generate plots that contain the key structurally-relevant features of real scattering signatures has not previously been demonstrated in the literature, and makes `mtPatterns` an effective tool for future cytometry research. Given that defects associated with mitochondria are implicated not only in carcinogenesis, but also with a number of neurodegenerative disorders [29], the use of this cytometric tool has the potential to improve our understanding and detection of these diseases.